

Compact nanohole/disk array-based plasmonic fiber-optic end-facet sensing probe: batch preparation and performance determination

Yijin He (何怡瑾)¹, Yuzhang Liang (梁瑜章)^{1*}, Xinran Wei (魏欣然)¹, Yuqi Du (杜雨琪)¹, Lanlan Shen (申岚岚)¹, Jingyuan Zhao (赵婧媛)², Cheng Yang (杨成)³, Yurui Fang (方蔚瑞)¹, and Wei Peng (彭伟)¹

¹School of Physics, Dalian University of Technology, Dalian 116024, China

²Department of Clinical Laboratory, Central Hospital of Dalian University of Technology, Dalian 116024, China

³School of Chemistry, Dalian University of Technology, Dalian 116024, China

*Corresponding author: yzliang@dlut.edu.cn

Received October 12, 2024 | Accepted December 18, 2024 | Posted Online May 16, 2025

A gold nanohole/disk array-based plasmonic fiber end-facet sensing probe is proposed and demonstrated experimentally, where the hybrid plasmon mode on the top surface used for sensing is excited by the cooperative effect of the near-field coupling between the nanohole and the nanodisk, as well as the localized surface plasmon of the nanodisk. The high-quality integration of the nanohole/disk array on the fiber end facet is achieved by combining nanoimprint lithography on a planar substrate with fiber ultraviolet (UV)-curable adhesive transfer techniques. As a result, the fabricated fiber probe experimentally exhibits a moderately high bulk refractive index sensitivity of ~ 196.91 nm/RIU and excellent surface sensitivity. Furthermore, the specific identification and determination of protein molecules verify their sensitivity analysis capabilities for future bioassays. This work provides a feasible plasmonic excitation strategy and enables batch-manufactured technology for nanostructure-based fiber probes to break through the current bottlenecks in biosensing applications.

Keywords: plasmonic fiber sensor; metallic nanostructure array; mode hybridization coupling; batch preparation; biomolecular detection.

DOI: [10.3788/COL202523.063601](https://doi.org/10.3788/COL202523.063601)

1. Introduction

Plasmonic fiber-optic end-facet devices, integrating functional nanostructures directly onto the small end facet of fiber, have garnered significant attention in various fields, including biochemical sensing^[1-4], light field manipulation^[5-7], high-resolution imaging^[8-10], and the like. The most striking feature of these nanostructure-based fiber end-facet devices is that they effectively combine the near-field enhancement of plasmonic nanostructures with both flexible spatial light-guiding and micro-sized end facets of the fiber. The miniature end-facet integration greatly simplifies the traditional benchtop microscope measurement system of micro-area nanostructures and makes the most of the fiber's remote small-area invasion capability. The fiber integration provides a light-coupled microscopic platform for remote, on-site, and point-of-care biochemical detection.

Benefiting from the success of plasmonic sensing technology and the maturity of the precision micro/nano preparation, numerous fiber end-facet devices with various nanostructure geometries and dimensions have been proposed and realized

experimentally through many specially developed nanofabrication techniques^[11-15]. However, there are still two critical challenges for the practical application. First, the plasmon mode at the perceptual surface of the nanostructure on the fiber end facet is generally not easily excited in the reflection operation mode. Even when excited on the fiber end facet, these plasmon modes typically exhibit low peak contrast, wide linewidth, and weak near-field enhancement. These issues restrict the practical application of the fiber sensor. Second, it is difficult to directly fabricate nanostructures upon the tiny fiber end facet using common planar nanofabrication techniques, including focused ion beam^[16], electro-beam lithography^[17], two-photon direct laser writing^[18], interference lithography^[19], femtosecond (FS) laser writing^[20], and tridimensional (3D) microprinting^[21], due to the incompatibility between the large-scale planar substrate and the tiny fiber tip. These direct preparation methods are high-cost, low-yield, and time-consuming.

To reduce the preparation cost and bypass the difficulty of direct patterning, a variety of novel nanofabrication techniques have been developed for optical fibers, including nanosphere

templating^[22], template transfer^[23,24], nanoskiving^[25], and self-assembly^[26]. Comparing these indirect methods in terms of preparation cost and process complexity, template transfer has emerged as the most promising technique for preparing nanostructures on fiber end-facets^[27-30]. Currently, transfer methods for patterning the optical fiber end facet are mainly divided into three categories: (1) directly transferring suspended plasmonic nanostructure membrane to the fiber end facet^[31]; (2) transferring plasmonic nanostructures on the planar substrate to the fiber end facet using ultraviolet (UV)-curable and heat-curable adhesives^[29]; (3) patterning the fiber end facet through the transfer method of hot-pressing and UV nanoimprinting, followed by the deposition of the metallic layer^[24]. However, most transfer methods merely focus on the preparation of a single fiber each time. This results in a low yield preparation and a lack of consistency among fiber probes, limiting the development of fiber end-facet sensing devices for bioassays. Therefore, there is a need to design a sensing probe that can be realized at a low cost and with efficient preparation while having good sensing performance.

In this paper, we propose to utilize a hybrid nanohole/disk array as a plasmonic sensing component and integrate it on the end facet of a multimode optical fiber through a combination of both template transfer and nanoimprint lithography. This combined procedure enables high-quality batch fabrication of 15 nanohole/disk array-based fiber probes at a time, with the assistance of optical fiber clamps, ensuring good spectral reproducibility among different fiber sensing probes. The fabricated plasmonic fiber probe exhibits a reflective resonant dip, primarily originating from the synergetic effect of the array-coupled surface plasmon polariton (SPP) and localized surface plasmon (LSP) of individual nanoholes at the top surface, perturbed by the near-field coupling between the nanohole and the nanodisk. Sensing detection results demonstrate that the fabricated plasmonic fiber probe demonstrates a moderate bulk refractive index (RI) sensitivity of ~ 196.91 nm/RIU and superior surface sensitivity due to its strong near-field localized capability. We further demonstrate the fiber probe's effectiveness as a biosensor for specifically detecting protein molecular Con A with a detection limit of 0.45 $\mu\text{g/mL}$.

2. Materials and Simulation Method

2.1. Materials

UV epoxy glue from Loctite 3311, operating at a wavelength of 395 nm, was purchased from Henkel Loctite New Materials (China) Co., Ltd. Poly (allylamine hydrochloride) (PAH), poly (sodium-p-styrenesulfonate) (PSS), and sodium chloride (NaCl) were obtained from Sigma-Aldrich Inc. 11-Mercaptoundecanoic acid (11-MUA), 1-(3-Dimethylaminopropyl)-3-ethylcarbodiimide (EDC, 155.241 Da), N-Hydroxy succinimide (NHS, 115.09Da), Concanavalin A (Con A), ribonuclease (Rnase B), bovine serum albumin (BSA), and phosphate-buffered saline (PBS) solution (pH 7.4) were purchased from Sangon Biotech Inc. The multimode optical fiber, with a numerical aperture

(NA) of 0.37, was purchased from Changfei Optical Fiber & Cable Co. Ltd. with specifications of 400/430/730 μm for core/cladding/coating diameters.

2.2. Simulation method

The 3D numerical simulation of the proposed plasmonic fiber optic probe is performed using the finite-difference time-domain (FDTD) method. The role of the optical fiber itself is not considered in the simulations, but a UV-cured adhesive with an RI of 1.5 is chosen as the substrate of the structure. This is because the thickness of the UV-cured adhesive is much larger than that of the nanostructure. At normal incidence, a plane wave of the Bloch/periodic type with an electric field along the y direction propagates from the fiber substrate side to the structural surface. Due to the inherent symmetry of the nanohole/disk array and its relation with the electric field direction of the incident light, symmetric and anti-symmetric boundary conditions are applied in both $\pm x$ and $\pm z$ directions to accelerate computation time and save computation memory. Meanwhile, perfectly matched layer conditions are imposed in the $\pm y$ directions. A refined mesh of $3.46 \text{ nm} \times 1 \text{ nm} \times 2 \text{ nm}$ along the x , y , and z directions is loaded in the gold (Au) region to obtain accurate results. Moreover, the permittivity of the Au material in the investigated wavelength range is obtained from Johnson and Christy^[32].

3. Results and Discussion

3.1. Geometric structure and the corresponding sensing mechanisms

The geometric structure of the proposed nanohole/disk array-integrated plasmonic fiber end-facet probe and its optical spectra are demonstrated in Fig. 1. A 3D structural schematic and a cross-section view are shown in Fig. 1(a). The plasmonic nanohole/disk array consists of top Au nanohole and bottom Au nanodisk arrays, arranged in a close-packed triangular lattice. Specific structural parameters include an array periodicity (P) of 450 nm, diameters (D) of the nanodisk and nanohole of 220 nm, and an Au layer's thickness (h_1) of 50 nm. Moreover, the height of the middle epoxy glue nanohole array (h_2) is set at 60 nm.

The simulated reflection spectrum is shown as the orange-filled curve in Fig. 1(b). Notably, the fiber probe is immersed in an aqueous solution with an RI of 1.3311. Obviously, there are two resonant dips observed at wavelengths of 627 and 719 nm, marked as D_1 and D_2 , respectively. Reflection dips D_1 and D_2 have respective linewidths of 39.2 and 28.1 nm. Based on their linewidths and wavelength positions, the Q -factors of these two dips are calculated as 15.9 and 25.6, respectively. As a direct comparison, the experimentally measured reflection spectrum is depicted as the blue-filled curve of Fig. 1(c). Similarly, two resonant dips are observed at 630 nm for dip D_1 and 708 nm for dip D_2 . The measured linewidth and Q -factor of the resonant dip at the dip D_1 (D_2) are 32.3 nm (32.4 nm) and 19.5 (21.9), respectively. In terms of

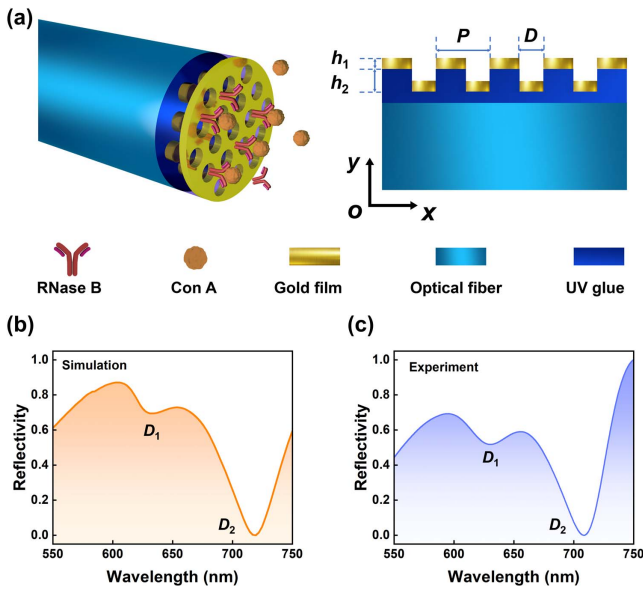


Fig. 1. The nanohole/disk array-integrated plasmonic fiber sensing probe: geometric structure and reflection spectra. (a) Schematic illustration of the hybrid nanohole/disk array on the end facet of the multimode fiber and its cross-sectional view with marked structural parameters. (b) Theoretically simulated [orange-filled curve] and (c) experimentally measured [blue-filled curve] reflection spectra of the nanohole/disk array-based fiber probe, where two reflection dips are marked by D_1 and D_2 .

spectral shape and the number of resonant dips, the measured spectrum exhibits good agreement with the counterpart in the simulation. However, some unavoidable discrepancies exist between them, such as the wavelength position and linewidth, mainly attributed to the surface roughness and slight variations in geometric and material parameters.

To elucidate the generation mechanism of dips D_1 and D_2 , Figs. 2(a)–2(d) depict electric and magnetic field profiles in the x - y plane (cross-section) at dips D_1 and D_2 , respectively. For dip D_1 , the electric field is mainly localized into three regions: two edges of the top surface of the nanohole, the middle nanogap between the nanohole and the nanodisk, as well as two

edges of the bottom surface of the nanodisk. Maximum electric field intensities for these three regions are almost the same, although the dip D_1 has a relatively high reflection intensity. Specifically, the generation process of dip D_1 can be described as follows: incident light first excites the LSP mode of individual nanodisks at the bottom side with a negligible array-coupled SPP at the Au film-UV adhesive glue interface. Then the plasmon mode at the top surface of the structure is generated by strong near-field coupling between the top nanohole and the bottom nanodisk because the incident light cannot directly irradiate the top surface due to the complete blocking of the structure. Therefore, dip D_1 mainly originates from the synergetic effect of the array-coupled SPP and LSP of an individual nanohole at the top surface, perturbed by the near-field coupling between the nanohole and the nanodisk, which is also the reason why the wavelength of dip D_1 is longer than that of ideal array-coupled SPP at the interface of the Au film and the measured sample. The enhanced optical field localized on the top surface makes dip D_1 sensitive to changes in ambient environments, which can be used for sensing applications.

Moreover, the intensity of the plasmon mode at the top surface of dip D_1 is determined by the coupling efficiency of the LSP at the bottom surface of the nanodisk. We notice that the electric field is patterned periodically along the horizontal direction at the incident region, which is attributed to low coupling efficiency and spatial interference of directly reflected light from the structure and dipolar radiation from the nanodisk. The magnetic field distribution in Fig. 2(c) is a more intuitive validation of this interpretation.

Compared to dip D_1 , the electric field profile at dip D_2 is mainly localized at the bottom surface of the structure. This is because the resonant dip D_2 mainly originates from the strong coupling of both the array-coupled SPP and LSP of the individual nanodisk at the bottom surface. Although the electric field is also rarely tunneled into both the nanogap and top surface, these field profiles have a weak influence on dip D_2 . Additionally, its field pattern inside the whole incident region disappears due to almost zero reflection from the structure. Since its electromagnetic field is mainly localized inside the substrate of UV glue and not in contact with the external solution to be measured, resonant dip D_2 is immune to the ambient environment, making it useful as a self-reference channel for dip D_1 .

Figures 2(e) and 2(f) give surface charge distributions at dips D_1 and D_2 , respectively, with the schematic on the left side clearly indicating calculated results on the right side. Here, we only focus on surface charge distribution along the horizontal direction and around these edges because the dipolar radiation cancels each other out from longitudinal charge for either a nanohole or a nanodisk. Obviously, electric charges on the left and right sides at the top and bottom surfaces of both nanoholes and nanodisks are just the opposite, which can be simplified as the interaction of electrical dipoles. Due to different generation mechanisms, we mainly focus on charges at the top surface for dip D_1 and the bottom surface for dip D_2 . Comparing Figs. 2(e) and 2(f), a noticeable difference between the two dips is that the surface charge at the bottom surface of the nanohole is just the

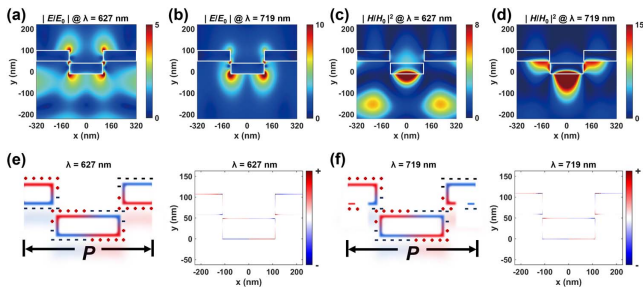


Fig. 2. The generation mechanism of two resonant dips of the nanohole/disk-integrated fiber end-facet probe. Normalized electric field distributions at (a) dip D_1 of 627 nm and (b) dip D_2 of 719 nm. Corresponding magnetic field distributions at (c) dip D_1 of 627 nm and (d) dip D_2 of 719 nm. Surface charge distributions of (e) dip D_1 and (f) dip D_2 , where the schematic of surface charge distribution on the left side clearly shows calculated results on the right side.

opposite, which can lead to the following statement: in the case of dip D_1 , the top surface of the hybrid structure can be regarded as an entire dipole. However, dip D_2 needs to be seen as the result of the interaction of two reversed dipoles. This charge distribution further verifies our interpretation: the LSP of the nanohole at the bottom surface is responsible for the generation of dip D_1 . However, dip D_2 stems from the strong coupling of the array-coupled SPP and LSP at the bottom surface, leading to a change in charge distribution.

3.2. Batch fabrication and structure characterization

Figure 3(a) shows the detailed preparation flow chart of the proposed plasmonic fiber probe, which mainly includes two main processes: one is to fabricate the hybrid nanohole/disk array on the planar polyethylene terephthalate (PET) substrate (top panel); the other is to transfer the hybrid nanohole/disk array from the PET substrate to the optical fiber end facet (bottom panel). The specific preparation procedure is described as follows: first, the 7-mm-diameter circular template of the nanohole array arranged on a 20.32 cm (8 in) silicon wafer in the squared lattice is fabricated using the combination technology of the 248 nm deep-UV lithography and inductively coupled plasmon etching. The interval between each circular pattern is 1 cm,

resulting in a total of 293 circular patterns on the 20.32 cm silicon wafer. The nanohole array in the triangular array possesses a periodicity/diameter/height of 450/220/60 nm, respectively. The UV nanoimprinting technique is then used to transfer the nanohole array on the silicon template into the UV-cured adhesive on the PET substrate, forming the complementary nanodisk array on the PET.

Afterward, an anti-adhesion layer is deposited on the surface of the nanodisk array-patterned PET substrate to facilitate the nanostructure transfer. Finally, a 50-nm-thick Au layer is deposited on the surface of a small piece of the prepared PET through a desktop magnetron sputtering coater. A photograph of a small piece of the nanostructured PET is shown in Fig. 3(b), where the centered red and marginal yellow regions correspond to the presence and absence of the Au nanodisk/hole array. The enlarged SEM image of the Au nanodisk/hole array is shown in Fig. 3(c). The homogeneous color of the macroscopic photograph and the local microscopic size of the nanostructure of the SEM image indicate that the designed nanostructure on the PET substrate is prepared successfully, laying the foundation for the subsequent preparation of the nanostructured fiber probe.

Based on the above preparation, the transferring of the nanohole/disk array from the PET substrate to the optical end facet is described as follows: first, the 400- μm -diameter end facet of a multimode optical fiber is obtained directly using customized fiber-optic cutting machines. Here, the advantage of the used multimode fiber with a core diameter of 400 μm can be found in Ref. [13]. Then, the whole fiber end facet is coated with a minimal amount of UV epoxy glue. After the optical fiber is mounted on a five-dimensional adjustable bracket, its end facet is contacted horizontally with an Au nanodisk/hole array on the PET. The horizontal alignment is achieved using the overlapping law of the object and mirror image with the help of two long-focus body microscopes with different orientations, as shown in Fig. 3(f). After the alignment, the UV epoxy glue is cured for 30 min with a UV light. The side- and top-view microscope photographs of the Au nanohole/disk array-patterned fiber end facet are shown in Fig. 3(d). Obviously, the entire fiber end facet is perfectly covered by the Au nanohole/disk array, demonstrating excellent flatness and smoothness and the feasibility of further processing. The nanohole/disk array-based fiber probe, packaged in an SMA905 fiber-optic connector, is shown on the left side of Fig. 3(e), with the enlarged SEM image on the right side of Fig. 3(e). It is clearly observed that the nanostructure array is just complementary to those in the PET substrate, as seen in the SEM image in Fig. 3(c).

To improve the preparation efficiency of plasmonic fiber probes and their consistency, we demonstrate the batch preparation of 15 fiber sensing probes at a time, as shown in Fig. 3(g). A total of 15 fibers are fixed with a customized optical fiber clamp and mounted on a five-dimensional adjustable bracket for the transferring process. Photographs in Fig. 3(g) show the batch-fabrication process and preparation results. Figure 3(h) presents the reflection spectra of 15 optical fibers prepared simultaneously. Distinctly, there is good spectral reproducibility among different fiber-sensing probes.

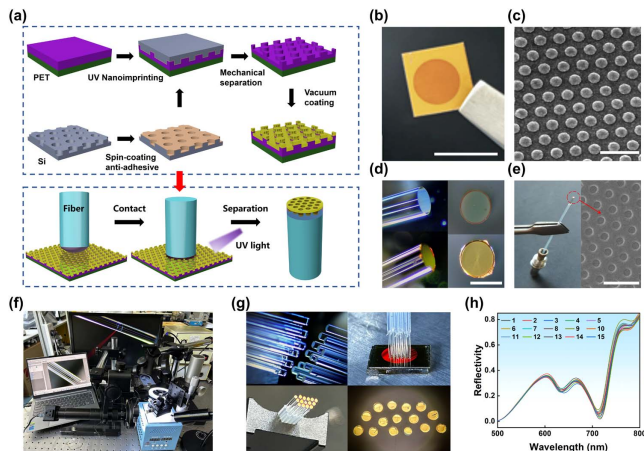


Fig. 3. Preparation process of the Au nanohole/disk array on the fiber end facet and the demonstration of fabrication results. (a) The whole fabrication procedure diagram includes two main sections: the fabrication of the large-scale Au nanohole/disk array on the flexible PET substrate and the transfer of the nanohole/disk array from the flexible planar substrate to the fiber end facet. (b) Photograph and (c) scanning electron microscope (SEM) image of the fabricated centimeter-scale Au nanohole/disk array on the flexible PET substrate. The scale bar is 10 mm in (b) and 1 μm in (c). (d) Side- and top-view microscope photographs of the fiber end facet before and after the transferring process. The scale bar is 400 μm . (e) A mobile phone photograph and SEM image of the fabricated fiber probe mounted in a fiber-optic connector. The scale bar is 1 μm . (f) A photograph of the home-built experimental setup for the transferring process. (g) Photographs showing the batch-fabrication process of 15-nanohole/disk array-based fiber probes, each time using a customized fiber bundle fixture. (h) Normalized reflection spectra of 15 fiber end-facet probes in a single preparation.

Table 1. Comparison of Different Fiber Optic Sensing Probes.

Ref.	Structure	Bulk RI sensitivity (nm/RIU)	Manufacturing technology	Cost	Manufacturing efficiency
[23]	Au disk-hole coupling structures	$S = 153$	Template transfer method	Low	Low
[26]	Au nanodisk array/thin film	$S = 137.28$	UV curing glue transfer technology	Low	Low
[35]	Au nanodot arrays	$S = 196$	Electron beam	High	Low
This work	Au nanohole/disk array	$S = 196.91$	Template transfer method	Low	High

as 40.12 nm, which indicates the excellent near-field enhancement characteristic for sensing detection. Equivalent simulated results are shown in Fig. 5(c) (red dots), where each PAH/PSS bilayer is equivalent to a 2.9-nm-thick dielectric layer with an RI of 1.56. Obviously, the variation tendencies are almost consistent with the experimental ones. After a comparison, it is found that the simulated decay length of 41.69 nm is a bit longer than the experimental one, and the increase in spectral depth dip D_1 is more pronounced with the increase in the number of bilayers.

To further demonstrate the biosensing capability of the fabricated plasmonic fiber probe, different concentrations of the protein Con A are detected specifically using the RNase B-functionalized fiber probe^[34]. The process of surface functionalization and detection is depicted in Fig. 5(d). Initially, a fiber probe is immersed in a 2 mmol ethanol solution of 11-mercaptoundecanoic acid and incubated at room temperature for 12 h to self-assemble a layer of carboxyl groups on its surface. After washing and drying, the carboxyl groups on the surface are activated using a mixture of aqueous solutions of EDC (0.5 mmol) and NHS (0.2 mmol) for 30 min at 4°C. After cleaning the surface again, the surface of the fiber probe is incubated in the PBS solution containing 0.1 mg/mL RNase B for 30 min at room temperature. To prevent non-specific binding, the surface is passivated again with a 1 mg/mL BSA solution for 30 min. Afterward, the surface-functionalized fiber probe is immersed sequentially in five concentrations of Con A solution, namely, 1, 2, 5, 10, 50, and 100 $\mu\text{g/mL}$ for 30 min, while the wavelength of dip D_1 is recorded in real time. As shown in Fig. 5(e), we observed a redshift of dip D_1 with increasing Con A concentrations. Figure 5(f) depicts a plot of wavelength redshift as a function of Con A concentration on a logarithmic scale, based on the spectra obtained for measuring Con A. The results exhibited a linear trend and demonstrated good agreement across the concentration range of 1 to 100 $\mu\text{g/mL}$. During the Con A capturing step, different concentrations of Con A can be discriminated successfully. The limit of detection (LOD) is determined to be 0.45 $\mu\text{g/mL}$. Furthermore, our sensors can be directly inserted into the body or confined spaces for detection, offering high detection sensitivity while enabling *in vivo* studies or *in situ* monitoring.

To demonstrate the advantage of our proposed Au nanohole/disk array-based plasmonic fiber probe, some detailed comparisons are made between our work and some previously reported

relevant works in terms of bulk RI sensitivity, manufacturing technology, cost, and manufacturing efficiency, which is summarized as Table 1. Comparison results show that our proposed fiber probe can achieve low cost and high manufacturing efficiency while ensuring sensing performance.

4. Conclusion

In summary, we have experimentally demonstrated an Au nanohole/disk array-based plasmonic fiber end-facet sensing probe, exhibiting two reflection resonant dips, only a short wavelength dip of which is suitable for sensing detection. This plasmonic nanostructure-based fiber probe has been prepared in batches by combining nanoimprint lithography and UV-curable adhesive transfer techniques, effectively reducing fabrication costs and accelerating preparation efficiency. Furthermore, the generation mechanisms of the resonant dip and the sensing performances of the proposed fiber probe are analyzed and evaluated systematically. The results show that the fabricated fiber probe possesses a moderately high bulk RI sensitivity of ~ 196.91 nm/RIU, excellent surface sensitivity, and detection capacity of protein Con A with a LOD of 0.45 $\mu\text{g/mL}$, which makes it promising in biochemical and environmental detection. This work offers a potential nanostructured fiber end-face probe and corresponding batch preparation method, which lays a solid foundation for future practical application of plasmonic fiber-optic probes.

Acknowledgements

This work was supported by the National Natural Science Foundation of China (Nos. 12274052 and 62171076), the Natural Science Foundation of Liaoning Province (No. 2022-MS-134), and the Fundamental Research Funds for the Central Universities (Nos. DUT24ZD203 and DUT23BK063).

References

1. Y. Chen, Q. Lin, H. Cheng, *et al.*, "Nanodiamond-based optical-fiber quantum probe for magnetic field and biological sensing," *ACS Sens.* **7**, 3660 (2022).
2. M. Sanders, Y. Lin, J. Wei, *et al.*, "An enhanced LSPR fiber-optic nanoprobe for ultrasensitive detection of protein biomarkers," *Biosens. Bioelectron.* **61**, 95 (2014).

3. M. Scaravilli, A. Micco, G. Castaldi, *et al.*, "Excitation of Bloch surface waves on an optical fiber tip," *Adv. Opt. Mater.* **6**, 1800477 (2018).
4. Y. Zhang, H. Wu, H. Wang, *et al.*, "Ultraminiature optical fiber-tip directly-printed plasmonic biosensors for label-free biodetection," *Biosens. Bioelectron.* **218**, 114761 (2022).
5. C. Li, T. Wieduwilt, F. J. Wendisch, *et al.*, "Metafiber transforming arbitrarily structured light," *Nat. Commun.* **14**, 7222 (2023).
6. M. Principe, M. Consales, A. Micco, *et al.*, "Optical fiber meta-tips," *Light Sci. Appl.* **6**, e16226 (2017).
7. C. Zhou, W. B. Lee, S. Gao, *et al.*, "All-dielectric fiber meta-tip enabling vortex generation and beam collimation for optical interconnect," *Laser Photonics Rev.* **15**, 2000581 (2021).
8. H. Feng, R. Zhu, and F. Xu, "Feature-enhanced fiber bundle imaging based on light field acquisition," *Advanced Imaging* **1**, 011002 (2024).
9. B. Li, C. Liao, Z. Cai, *et al.*, "Femtosecond laser 3D printed micro objective lens for ultrathin fiber endoscope," *Fundam. Res.* **4**, 123 (2024).
10. H. Ren, J. Jang, C. Li, *et al.*, "An achromatic metafiber for focusing and imaging across the entire telecommunication range," *Nat. Commun.* **13**, 4183 (2022).
11. S. Bian, M. Shang, and M. Sowan, "Rapid biosensing SARS-CoV-2 antibodies in vaccinated healthy donors," *Biosens. Bioelectron.* **204**, 114054 (2022).
12. G. Kostovski, P. R. Stoddart, and A. Mitchell, "The optical fiber tip: an inherently light-coupled microscopic platform for micro- and nanotechnologies," *Adv. Mater.* **26**, 3798 (2014).
13. Y. Liang, Z. Yu, L. Li, *et al.*, "A self-assembled plasmonic optical fiber nanoprobe for label-free biosensing," *Sci. Rep.* **9**, 7379 (2019).
14. M. Pisco and A. Cusano, "Lab-on-fiber technology: a roadmap toward multifunctional plug and play platforms," *Sensors* **20**, 4705 (2020).
15. Y. Xiong and F. Xu, "Multifunctional integration on optical fiber tips: challenges and opportunities," *Adv. Photonics* **2**, 064001 (2020).
16. A. Dhawan, M. D. Gerhold, and J. F. Muth, "Plasmonic structures based on subwavelength apertures for chemical and biological sensing applications," *IEEE Sens. J.* **8**, 942 (2008).
17. Y. Lin, J. Guo, and R. G. Lindquist, "Demonstration of an ultra-wideband optical fiber inline polarizer with metal nano-grid on the fiber tip," *Opt. Express* **17**, 17849 (2009).
18. W. Hadibrata, H. Wei, S. Krishnaswamy, *et al.*, "Inverse design and 3D printing of a metalens on an optical fiber tip for direct laser lithography," *Nano Lett.* **21**, 2422 (2021).
19. S. Feng, X. Zhang, H. Wang, *et al.*, "Fiber coupled waveguide grating structures," *Appl. Phys. Lett.* **96**, 133101 (2010).
20. C. Li, Y. Liu, C. Lang, *et al.*, "Femtosecond laser direct writing of a 3D micro-cantilever on the tip of an optical fiber sensor for on-chip optofluidic sensing," *Lab Chip* **22**, 3734 (2022).
21. M. Zou, C. Liao, S. Liu, *et al.*, "Fiber-tip polymer clamped-beam probe for high-sensitivity nanoforce measurements," *Light Sci. Appl.* **10**, 2047 (2021).
22. X. Li, F. Wang, X. Wang, *et al.*, "Plasmonic-photonic hybrid configuration on optical fiber tip: toward low-cost and miniaturized biosensing probe," *Sens. Actuators B. Chem.* **367**, 132059 (2022).
23. S. Li and W. Li, "Refractive index sensing using disk-hole coupling plasmonic structures fabricated on fiber facet," *Opt. Express* **25**, 29380 (2017).
24. P. Jia, D. Kong, and H. Ebendorff-Heidepriem, "Resist-free nanoimprinting on optical fibers for plasmonic optrodes," *Appl. Mater. Today* **20**, 100751 (2020).
25. D. J. Lipomi, R. V. Martinez, M. A. Kats, *et al.*, "Patterning the tips of optical fibers with metallic nanostructures using nanoskiving," *Nano Lett.* **11**, 632 (2011).
26. H. H. Jeong, N. Erdene, J. H. Park, *et al.*, "Real-time label-free immunoassay of interferon-gamma and prostate-specific antigen using a fiber-optic localized surface plasmon resonance sensor," *Biosens. Bioelectron.* **39**, 346 (2013).
27. H. He, X. Wei, Y. He, *et al.*, "Plasmonic resonance coupling of nanodisk array/thin film on the optical fiber tip for integrated and miniaturized sensing detection," *Sensors* **23**, 4163 (2023).
28. X. He, H. Yi, J. Long, *et al.*, "Plasmonic crystal cavity on single-mode optical fiber end facet for label-free biosensing," *Appl. Phys. Lett.* **108**, 231105 (2016).
29. P. Jia and J. Yang, "A plasmonic optical fiber patterned by template transfer as a high-performance flexible nanoprobe for real-time biosensing," *Nanoscale* **6**, 8836 (2014).
30. X. Sun, Z. Lei, H. Zhong, *et al.*, "A quasi-3D Fano resonance cavity on optical fiber end-facet for high signal-to-noise ratio dip-and-read surface plasmon sensing," *Light Adv. Manuf.* **3**, 665 (2022).
31. Y. Wang, F. Liu, and X. Zhang, "Flexible transfer of plasmonic photonic structures onto fiber tips for sensor applications in liquids," *Nanoscale* **10**, 16193 (2018).
32. P. B. Johnson and R. W. Christy, "Optical constants of the noble metals," *Phys. Rev. B* **6**, 4370 (1972).
33. F. Li, J. Shen, C. Guan, *et al.*, "Exploring near-field sensing efficiency of complementary plasmonic metasurfaces for immunodetection of tumor markers," *Biosens. Bioelectron.* **203**, 114038 (2022).
34. Y. Liang, W. Cui, L. Li, *et al.*, "Large-scale plasmonic nanodisk structures for a high sensitivity biosensing platform fabricated by transfer nanoprinting," *Adv. Opt. Mater.* **7**, 1801269 (2019).
35. Y. Lin, Y. Zou, Y. Mo, *et al.*, "E-beam patterned gold nanodot arrays on optical fiber tips for localized surface plasmon resonance biochemical sensing," *Sensors* **10**, 9397 (2010).